

# Spectral analyses of basement rocks in El-Sibai-Umm Shaddad area, Central Eastern Desert, Egypt, using ASTER thermal infrared data

Safaa M. Hassan · Mohamed F. Sadek ·  
Reinhard O. Greiling

Received: 22 July 2014 / Accepted: 19 November 2014 / Published online: 30 November 2014  
© Saudi Society for Geosciences 2014

**Abstract** Advanced Spaceborne Thermal Emission and Reflection Radiometer (ASTER) level 1B (five thermal infrared (TIR) bands) data have been used to discriminate the exposed rock units in the Wadi El-Sibai-Umm Shaddad area in the Central Eastern Desert of Egypt. The quantitative and qualitative spectral characteristic analyses of the exposed rock units have been applied using the data of ASTER TIR bands (8–12  $\mu\text{m}$ ) in order to explain the relationship between emissivity of these rock units and their mineralogical composition. The exposed rock units comprise a variety of granitic rocks intruded into the ophiolitic and island arc metavolcanic assemblages of the Pan-African basement. The ophiolitic serpentinites talc-carbonate rocks, metavolcanics and granitic rocks are well discriminated by applying the ASTER thermal band ratios (12/13,  $10 \times 11/13 \times 14$ , 12/14) in RGB. In this study, the principal component analyses (PCA) of the five ASTER thermal bands are applied for the first time to discriminate the basement rocks in the study area. The method effectively discriminates between three granitic varieties forming the El-Sibai-Abu El Tiyur intrusion. They are biotite granite, leucocratic alkali-feldspar granite and riebeckite granite. These granitic varieties were previously mapped as one unit, namely alkali-feldspar granite. This study

reveals that the applied data of ASTER thermal ratio bands produced a new geological map with well-discriminated rock units.

**Keywords** El-Sibai-Umm Shaddad · Pan-African basement · Egypt · Emissivity spectra · ASTER · Thermal infrared · PCA

## Introduction

The El-Sibai-Umm Shaddad study area is located in the Central Eastern Desert of Egypt and covers about 853 km<sup>2</sup> (Fig. 1). It pertains to the northern part of the Pan-African Arabian Nubian Shield, which was formed by suturing of arc terranes consisting of arcs, accretionary prisms and back-arc basins that formed in the Mozambique Ocean (e.g. Stern 1994; Johnson et al. 2011). The Central Eastern Desert of Egypt is essentially a collage of tectonically assembled ophiolitic mélange and intraoceanic arcs, which were covered—later on—by molasse-type sediments and continental volcanics, and intruded by suites of granitoids and dyke swarms (El Ramly 1972; El Gaby et al. 1988 and 1990; Greiling et al. 1994). The lithological units in the Central Eastern Desert of Egypt have been studied using Landsat TM, Landsat Enhanced Thematic Mapper Plus (ETM+) and Landsat 8 (e.g. Gad and Kusky 2006; Hassan and Ramadan 2014). Gabal El-Sibai area was previously investigated using the Landsat TM images (Ragab et al. 1993; Tolba et al. 2003).

Landsat 8 has 11 spectral bands, covering the visible near-infrared bands (1–9), short-wave infrared bands (6 and 7) and only two thermal infrared bands with spatial resolution of 90 m (10 and 11) reflectance data. On the other hand, Advanced Spaceborne Thermal Emission and Reflection Radiometer (ASTER) covers a wide spectral region with 14 bands from the visible to the thermal infrared (Table 1). Several studies have demonstrated the usefulness of remotely

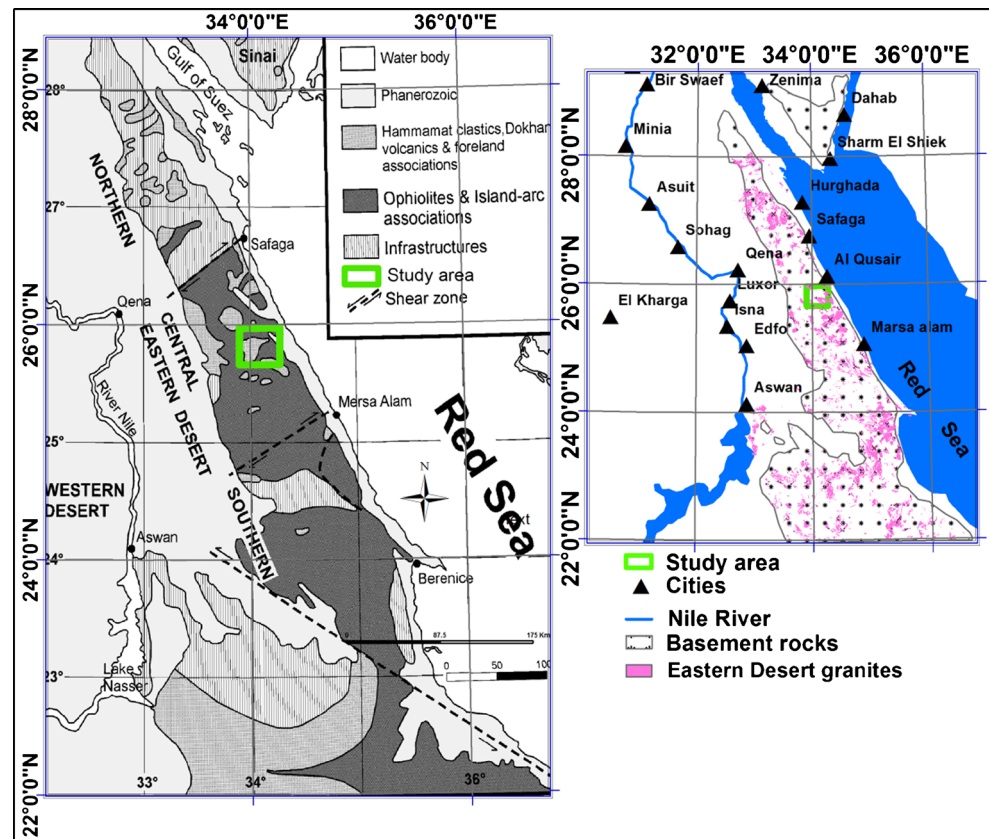
**Electronic supplementary material** The online version of this article (doi:10.1007/s12517-014-1729-8) contains supplementary material, which is available to authorized users.

S. M. Hassan (✉) · M. F. Sadek  
National Authority for Remote Sensing and Space Sciences  
(NARSS), Cairo, Egypt  
e-mail: Safaa.hassan@narss.sci.eg

S. M. Hassan  
e-mail: safaamh2002@yahoo.com

R. O. Greiling  
Institut für Angewandte Geowissenschaften, Karlsruhe Institute of  
Technology, Karlsruhe Universität, Karlsruhe, Germany

**Fig. 1** **a** Regional geological map of the Eastern Desert of Egypt (after El Gaby et al. 1988) illustrating the study area. **b** The location map of the study area shows the distribution of the basement and granitic rocks in the Eastern Desert of Egypt



sensed data for lithologic identification and geological mapping using both short-wave infrared (SWIR) and thermal infrared data (TIR ASTER) (e.g. Cudahy et al. 2000; Rowan and Mars 2003; Rowan et al. 2003; Ninomiya et al. 2005;

Hook et al. 2005; Mars and Rowan 2006; Gad and Kusky 2007; Le Yu, et al. 2008; Amer et al. 2010; Ali-Bik et al. 2012; Amer, et al. 2012; Sadek and Hassan 2012; Abou Elmagd et al. 2013; Rajendran et al. 2013). The three visible near-infrared bands (VNIR) are important sources of information related to absorption by transition elements especially iron and some rare earth elements (Rowan et al. 2003). Other studies have been focused on the use of remotely sensed data covering the thermal infrared (8–13  $\mu\text{m}$ ) in lithologic identification and geological mapping using multi-band TIR of ASTER (Ninomiya 2002; Ninomiya and Fu 2002 and 2003; Ninomiya et al. 2005; Vaughan et al. 2005; Moghtaderi et al. 2007; Le Yu et al. 2008; Aboelkhair et al. 2010).

The ASTER thermal data has not previously been applied in lithological mapping of Gabal El-Sibai area. The main scope of the present study is discrimination of the exposed rock units on the basis of their mineralogical compositions using the data of ASTER thermal band ratioing and principal component analyses.

### Geological setting

The early studies of Sabet (1961) on Gabal El-Sibai area indicated low- to medium-grade metamorphism of the schists

**Table 1** Characteristics of ASTER data

| Radiometric | Ground resolution | Spectral region | Spectral range ( $\mu\text{m}$ ) | Band number |
|-------------|-------------------|-----------------|----------------------------------|-------------|
| 8 bits      | 15 m              | VNIR            | 0.52–0.60                        | Band 1      |
|             |                   |                 | 0.63–0.69                        | Band 2      |
|             |                   |                 | 0.78–0.86                        | Band 3-N    |
|             | 30 m              | SWIR            | 0.78–0.86                        | Band 3-B    |
|             |                   |                 | 1.60–1.70                        | Band 4      |
|             |                   |                 | 2.145–2.185                      | Band 5      |
|             |                   |                 | 2.185–2.225                      | Band 6      |
|             |                   |                 | 2.235–2.285                      | Band 7      |
|             |                   |                 | 2.295–2.365                      | Band 8      |
| 12 bits     | 90 m              | TIR             | 2.360–2.430                      | Band 9      |
|             |                   |                 | 8.125–8.475                      | Band 10     |
|             |                   |                 | 8.475–8.825                      | Band 11     |
|             |                   |                 | 8.925–9.275                      | Band 12     |
|             |                   |                 | 10.25–10.95                      | Band 13     |
|             |                   |                 | 10.95–11.65                      | Band 14     |

with amphibolites which were derived from sediments and volcanics. El Ramly (1972) preferred a metasedimentary origin for the hornblende schists forming the infrastructure in the El-Sibai area. The El-Sibai gneisses have been described by El Gaby (1983) and El Gaby et al. (1984, 1988) as pre-Neoproterozoic crust remobilized in the Neoproterozoic–Early Paleozoic (900–520 Ma) during overthrusting of ensimatic cover nappes. In agreement with this, the infrastructure-suprastructure model was proposed for the El-Sibai complex by Kamal El Din et al. (1992), Kamal El Din (1993) and Khudeir et al. (1992, 1995). The oldest unit was described as an amphibolite–migmatite complex by Kamal El Din et al. (1992). Geochemically, Kamal El Din (1993) considered the amphibolites to have had a metasedimentary origin pertaining to island arc tholeiitic basalt.

The structural history of the El-Sibai complex was divided into eight deformational phases by Khudeir et al. (1992) and Kamal El Din (1993). The core of the Deleihimi antiform to the east of the Sibai is occupied by high-temperature gneisses and schist (El Gaby et al. 1994). Folding is responsible for the structure of the Sibai complexes (Hamimi 1996, Abdeen and Greiling 2005), while the SE margin of the gneissic complex is represented by a low-angle normal fault (Bregar et al. 1996) and folded thrust (Ibrahim and Cosgrove 2001). Fritz and Messner (1999), Fritz et al. (2002) and Bregar et al. (2002) applied the Meatiq metamorphic core complex model to the El-Sibai complex. El-Sibai intrusion was mapped as post-tectonic alkaline granitoids intruding the surrounding metavolcanics and older granitoids (EGSMA 1992). Fowler et al. (2007) revealed that the gneissic association rocks are not infrastructural, but they form a unit within the ophiolitic association nappes and that the El-Sibai is not antiformal in structure. Abdeen et al. (2014) divided the exposed rocks forming El-Sibai-Umm Gheig area into lower tier composed mainly of amphibolite–migmatite and granitoid gneisses and an upper tier of ophiolitic rocks, metavolcanics and their related volcanoclastics and molasse-type Hammamat sediments.

The exposed rock assemblages in the El-Sibai-Umm Shaddad area in the Central Eastern Desert of Egypt are related to the late Neoproterozoic, Pan-African tectono-magmatic episodes. The area is essentially composed of metavolcanic schist, metagabbros and serpentinites talc-carbonate rocks constituting the ophiolitic mélange of Shackleton (1979). This association is overlain by Hammamat molasse sediments. The whole association is intruded by syn- to late- to post-tectonic granitic intrusions including tonalite–granodiorite, monzogranites and alkali granites (cf. Fig. 7). In this study, three main assemblages of rock units are discerned: (1) ophiolitic rocks, (2) calc-alkaline metavolcanics and their related volcanoclastics and (3) intrusive rocks.

Ophiolitic assemblage (serpentinite and talc-carbonate rocks)

The ophiolitic assemblage consists of dismembered slabs of massive serpentinites and talc-carbonates, which were formed in a back-arc basin setting (Khudeir and Asran 1992). The serpentinites are exposed east of Gabal El-Sibai as N–S-trending lenticular bodies which are tectonically thrust over highly sheared metavolcanics and locally intruded by Nusla alkali-feldspar granite. The sheared talc-carbonate rocks crop out at the northern side of Wadi Umm Gheig, forming scattered slices within the schistose metavolcanics. The ophiolitic rocks were emplaced over the metavolcanics by remarkable NNW–SSE-trending thrusts, which were affected by folding of these rocks (Fig. 2a). The exposed serpentinite rocks are generally sheared and dissected by networks of magnesite veins and are locally associated with talc graphite schist slices and talc ankerite-silica (listwaenite) bodies. Ophiolitic slabs are locally incorporated within the sheared metavolcanics.

Schistose metavolcanics and metavolcanoclastics

The schistose metavolcanics and metavolcanoclastics are the dominant rock unit along Wadi Umm Gheig and in the eastern and the northern parts of Gabal El-Sibai. The Umm Gheig metavolcanic belt is frequently interleaved with serpentinite talc-carbonate rocks in the form of wedges or slices usually in association with bluish-grey talc-graphite schists. These serpentinites have sharp tectonic contacts with the surrounding metavolcanics.

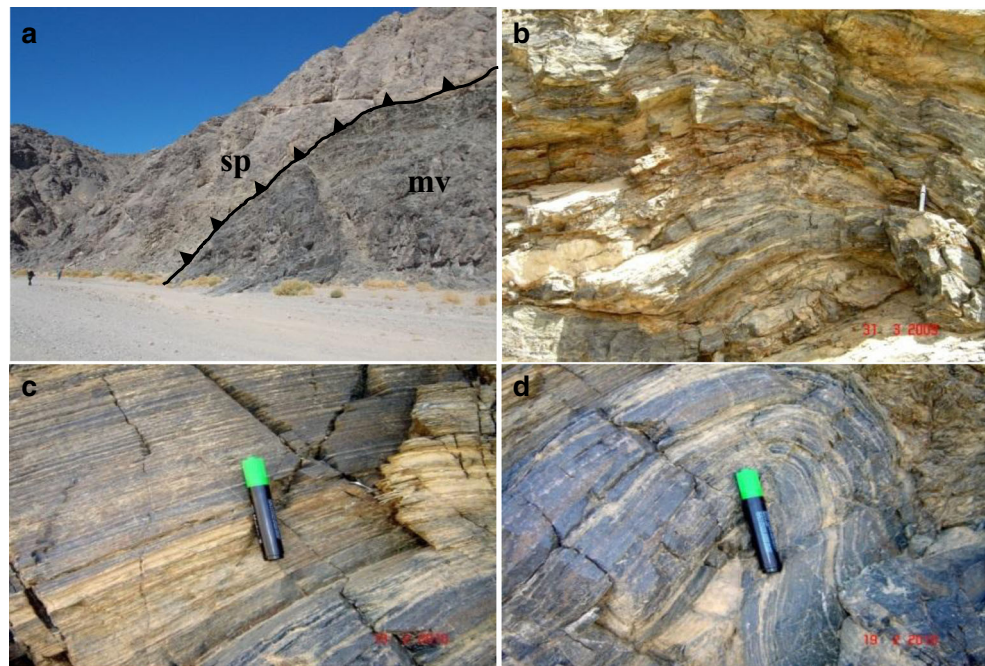
These rocks are basic to intermediate in composition and include chlorite hornblende schist showing greenschist facies metamorphism, though some rocks reach amphibolite facies. They are overthrust by slabs of talc-carbonate rocks. The whole belt is elongated in the NW–SE direction with remarkable macroscale folds and crenulations (Fig. 2b) and included a mega-scale open fold in Wadi Umm Lusseifa (Fig. 2c, d).

Intrusive rocks

The ophiolitic and island arc calc-alkaline metavolcanics are intruded by three different generations of granitoids: (a) El-Shush syn-magmatic gneissic tonalite–granodiorite, (b) Umm Shaddad–Delehimmi alkali-feldspar granite and (c) El-Sibai–Abu Tiyur late- to post-magmatic alkali granites (Kamal El Din 1993, Fowler et al. 2007).

1. The El-Shush gneissic tonalite–granodiorite forms a NW–SE-trending elongate intrusion. The gneissosity in this granite is weakly developed (Fowler et al. 2007). Flow banding and flow-oriented feldspar phenocrysts are observed in the lower more heterogeneous parts of the El-Shush intrusion. The transition from the El-Shush tonalite

**Fig. 2** **a** Ophiolitic serpentinites (*sp*) thrusting over schistose metavolcanics (*mv*) (SW-dipping thrust contact), Wadi Umm Lusseifa. **b** Wadi Umm Gheig strongly deformed, highly tectonized metavolcanics showing folding and crenulation. **c** Primary bedding in metavolcaniclastic rocks, Wadi Umm Lusseifa. **d** Folding in metavolcaniclastic rocks, Wadi Umm Lusseifa. The photo shows the dark hornblende-rich bands alternating with light felsic-rich bands



- into tonalite gneiss is marked by conformable bands of varying mafic mineral contents (Khudeir et al. 1995).
- The Umm Shaddad and Delihimmi alkali-feldspar granitoids intruded the metavolcanic assemblages. They have been mapped as alkali granites (EGSMA 1992) and as granites (Khudeir et al. 1995). Fowler et al. (2007) mapped Umm Shaddad intrusion as alkali granite and Delihimmi as granodiorite. Bregar et al. (1996) mentioned that the Umm Shaddad intrusion shows a gently SE dipping tabular geometry constrained by low-angle normal faults that controlled its intrusion. The Umm Shaddad and related red granites are mainly alkali-feldspar granites associated with syenogranites with high K-calc-alkaline affinity (El-Sayed et al. 1999). Sometimes, these rocks show schlieren and gneissic texture with flow-aligned large microcline phenocrysts.

The Delihimmi alkali-feldspar granite intrusion was identified by EGSMA (1992) as alkali granite, while Hamimi (1996) recognized it as a gneissic body and an extension of the gneissic association exposed in the core of an anticlinal structure. Akaad and Abu El Ela (2002) regarded the Delihimmi intrusion as younger granite, while Fowler et al. (2007) mapped this intrusion as gneissic granodiorite.

- El-Sibai-Abu Tiyur-El-Atawi late- to post-magmatic intrusions form a ring-shaped intrusion at the northern western part of the mapped area. They mainly comprise alkali-feldspar granites, in parts associated with syeno-granite. These rocks represent the youngest granitic varieties

intruded into the metavolcanics, gneissic tonalite and granodiorite. They are intersected by a group of faults trending mainly NW and NE and are traversed by quartz and fluorite veins and small pegmatitic patches. These rocks are related to the G3 granites of Hussein et al. (1982) and considered as A-type granites by Abdel-Rahman and El-Kibbi (2001) and El-Sayed et al. (2002) or as Late Cryogenian-Ediacaran granitoids of Johnson et al. (2011). The El-Sibai-Abu Tiyur granitic intrusion shows a wide variation in its mineralogical composition, including monzogranites, syenogranites and alkali granites. Petrographically, these granitic rocks are subdivided by Kamal El Din (1993) into (1) biotite granite which occupies the eastern and western parts of Gabal El-Sibai; (2) leucocratic alkali-feldspar granite forming the entire ring of the El-Sibai intrusion (Fowler et al. 2007); and (3) riebeckite granite occurring at the eastern part and the southern rim of the El-Sibai ring, which consists essentially of K-feldspars and Na-plagioclase, with subordinate amounts of quartz, riebeckite, aegirine and biotite. Ragab et al. (1993) suggested that the presence of some riebeckite needles and flakes enclosed in as well as on the expense of large biotite crystal may be due to post-magmatic sodic metasomatism. All of these basement rocks are traversed by many dykes and quartz veins with variable trends, lengths and widths. They are mafic, felsic and trachytic in composition.

## Materials and methods

### TIR spectra of the exposed rock units

One scene of ASTER level 1B covering the study area dated on 7 April 2007 “radiance at-sensor data” has been used with and without atmospheric correction (Ninomiya et al. 2005) in order to propose indices of the exposed rock units and improve the extraction of different lithological aspects. The ASTER scene was processed and analysed using Earth Resources Data Analyses System (ERDAS) IMAGINE version 2014. Five ASTER thermal bands with 90-m spatial resolution TIR data were geometrically corrected and resampled applying nearest neighbour resampling method to maintain the original pixel values of the image. Quantitative analyses have been applied to the ASTER thermal bands using ERDAS IMAGINE spectral profile viewer. Finally, the ASTER data was interpreted to produce the geological map. The spectral profile viewer of the image processing software (ERDAS IMAGINE, version 2013) allows user to visualize the reflectance or emission spectrum of a single pixel throughout many bands. This kind of image processing technique is particularly useful for multi-spectral data that have several layers. It allows estimation of the mineralogical composition of the material in the pixel. In the present study, the average of thermal spectral values of the mapped rock units are listed in Table 2, and the thermal characteristic curves have been delineated (different pixels) representing the exposed rock units (Fig. 3a–e) and the average values are defined. The average spectral curves of these rocks are also compared (Fig. 3f).

### Converting to emissivity and temperature

Before converting the ASTER thermal data to emissivity and temperature, atmospheric correction for ASTER level 1B “radiance at-sensor data” (8 to 14  $\mu\text{m}$ ) bands was applied to approximate and remove the atmospheric contributions from thermal infrared radiance data using ENVI version 5.1 software. ENVI emissivity normalization technique was applied to the five ASTER thermal bands to separate the emissivity values of the exposed rock units (Fig. 4).

### ASTER thermal band ratioing

Band ratioing is a helpful technique that can be applied for the discrimination of surface materials. The basic idea of this technique is to emphasize or exaggerate the anomaly of the target object (Abrams et al. 1983). This technique is typically used to enhance the spectral differences between surface materials that are difficult to detect in raw images (Aboelkhair et al. 2010). For discrimination of the widely exposed rock units in the study area using ASTER thermal data, many referenced and unreferenced band ratios have been tested. The ratios (Fig. 5)  $b_{10} \times b_{11} / b_{13} \times b_{14}$  for granitic rocks,  $b_{12} / b_{14}$  for metavolcanics and  $b_{12} / b_{13}$  for serpentinite talc-carbonate rocks have been selected based on the characteristic analyses of thermal spectrum of these rock units (Fig. 3).

### Principal component analysis transformation

Principal component analysis (PCA) transformation technique has been applied to the five derivative ASTER emissivity bands as a method of data compression and to reduce redundant information in highly correlated bands (Fig. 6). It allows redundant data to be compacted into fewer bands, that is, the dimensionality of the data is reduced. The bands of PCA data are non-correlated and independent and are often more interpretable than the source data.

In the present study, the PCA transformation was carried out on the five ASTER thermal images of the ophiolitic serpentinite and talc-carbonate, schistose metavolcanics and granitic intrusions. The obtained PCA eigenvector loadings and eigenvalues show that the first, second and third principal components (PCs) account for most of the total data variance (Table 3 and Fig. 6).

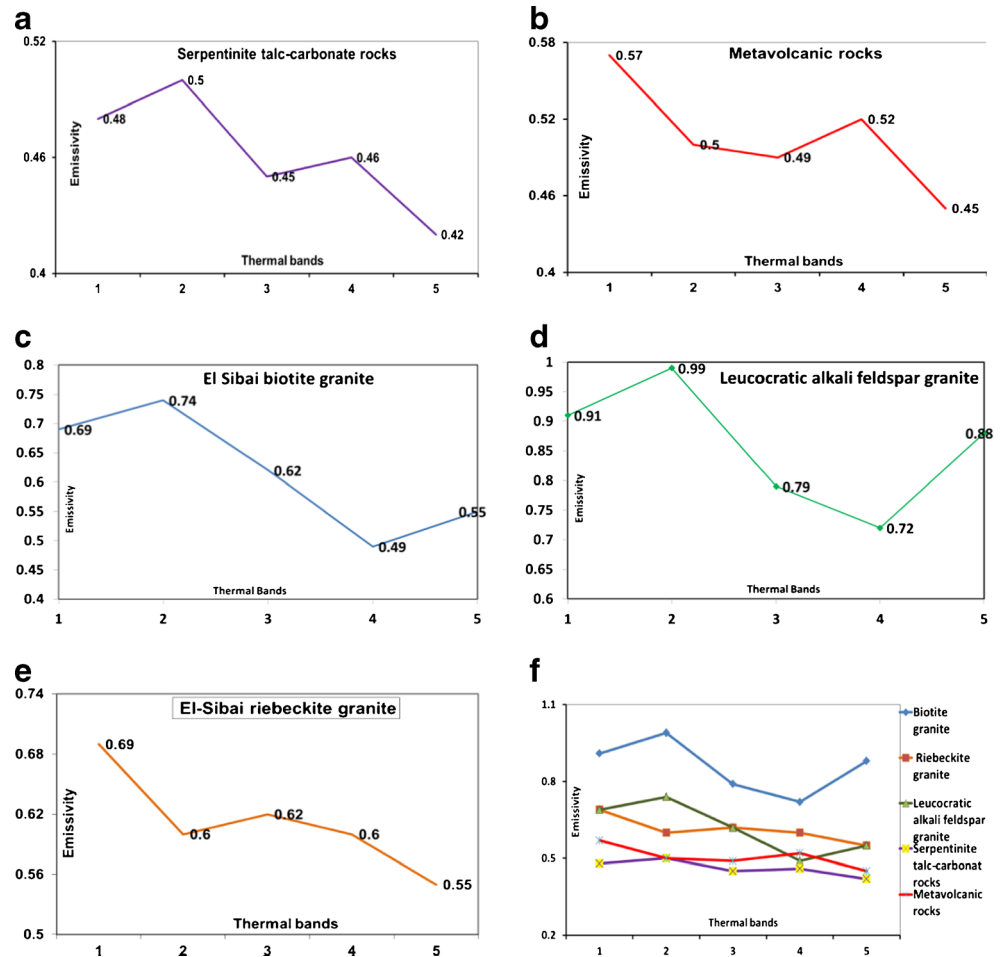
### Fieldwork

The produced geological map of the area, using the processed ASTER thermal images, was revised and verified through two field trips, whereas the different lithological units and their contacts have been checked with emphasis on the Gabal El-

**Table 2** The average ASTER thermal values for the main exposed rock units in the study area

| Rock types<br>ASTER bands | Ophiolitic (serpentinite-<br>talc-carbonate rocks) | Metavolcanics | Biotite granite | Leucocratic alkali-<br>feldspar granite | Riebeckite granite<br>(alkaline granites) |
|---------------------------|--|---------------|-----------------|---|---|
| 10                        | 0.48   | 0.57          | 0.69            | 0.91                                    | 0.69                                      |
| 11                        | 0.50   | 0.50          | 0.74            | 0.99                                    | 0.60                                      |
| 12                        | 0.45   | 0.49          | 0.62            | 0.79                                    | 0.62                                      |
| 13                        | 0.46   | 0.52          | 0.49            | 0.72                                    | 0.60                                      |
| 14                        | 0.42   | 0.45          | 0.55            | 0.88                                    | 0.55                                      |

**Fig. 3** The average ASTER TIR spectral curves characterizing the exposed rock units in study area. **a** Serpentine talc-carbonate rocks. **b** Metavolcanic rocks. **c** El-Sibai biotite granite. **d** El-Sibai leucocratic alkali-feldspar granite. **e** El-Sibai riebeckite granite. **f** TIR spectral curve of the widely exposed rock units



Sibai-Abu El Tiyur pluton. The structural features such as thrust and normal faults and lineaments have been checked, and many representative field photographs showing some field observations have been taken.

## Results and discussions

The igneous rocks are composed mainly of silicate minerals which do not show any spectral feature in VNIR or SWIR ASTER bands. They have pronounced spectral features in the TIR region due to asymmetric Si–O–Si stretching vibrations (Le Yu et al. 2008). Ninomiya et al. (2005) proposed that the series of the alkali-feldspar, which often coexist with quartz in felsic igneous rocks, have lower emissivity in band 11 than in bands 10 and 12, contrary to the quartz characteristics through the ASTER thermal band.

Petrographically, Kamal El Din (1993) identified three granitic varieties forming El-Sibai-Abu Tiyur late tectonic intrusion without discrimination on his geological map. In all previous geological maps, this intrusion was mapped as one granitic type, namely alkali-feldspar granite (e.g. EGSM

1992; Kamal El Din 1993; Abdel-Rahman and El-Kibbi 2001; Fowler et al. 2007). Based on the spectral characteristic analyses of principal component (PCA) of the five ASTER thermal bands (Table 3 and Fig. 6) as well as the field verification, the boundaries between these three petrographical varieties are clearly discriminated in this image as well as on the present geological map (Fig. 7).

The new three discriminated granitic varieties are described as follows:

1. Biotite granite forms the main mass of Gabal El-Sibai and well exposed in the western part of Gabal El-Sibai-Abu Tiyur intrusion. It consists essentially of quartz, plagioclase, K-feldspar and biotite. These rocks show higher thermal values in ASTER band 11 than in bands 10 and 12 due to their enrichment with quartz and low content of alkali-feldspar minerals (Fig. 3c and Table 2). Biotite granite can be discriminated by its very bright colour in the derivative emissivity image (Fig. 4a).
2. Leucocratic alkali-feldspar granite (Fig. 3d) is very poor in mafic minerals and consists essentially of microcline, micropertite and subordinate quartz. The thermal value in band 11 is higher than in both bands 10 and 12 due to the low

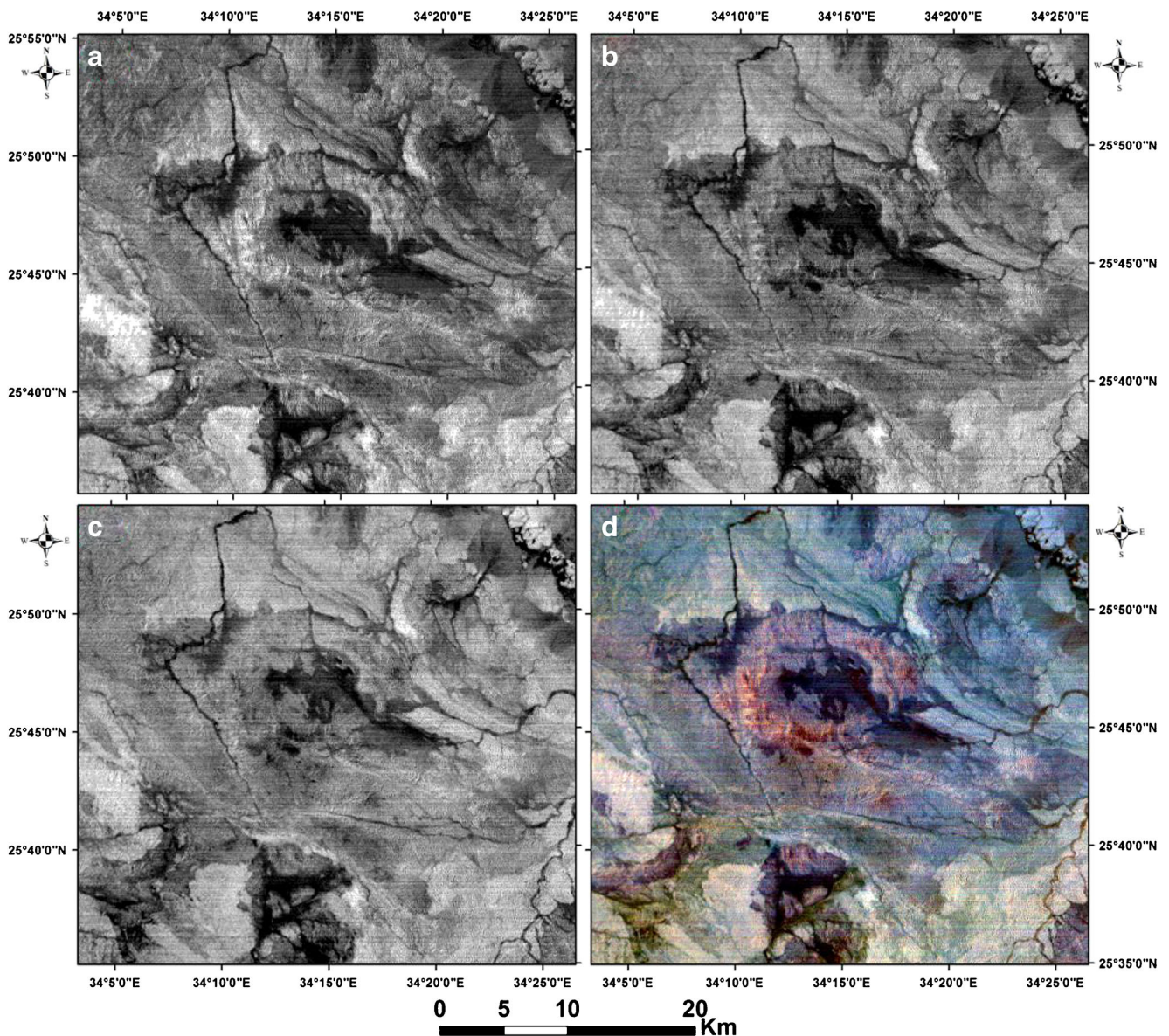


**Fig. 4** **a** Biotite granite has a higher emissivity value (*bright colour*) in band 11. **b** Riebeckite granite and alkali-feldspar granite show nearly the same emissivity values (*dark grey colour*) in band 10. **c** Leucocratic

alkali-feldspar granite exhibits *light grey colour* in band 12. **d** False colour composite emissivity image (b10, b11 and b12) in RGB

content of quartz. This granitic type is emphasized by light grey colour in band 12 in the derivative emissivity image (Fig. 4c).

3. Riebeckite granite intrudes the eastern part of El-Sibai-Abu Tiyur circular mass, the southern rim of Gabal El-Sibai and Wadi El-Shush nappe assemblage (Fig. 3e). It consists essentially of K-feldspars and Na-plagioclase, with subordinate assemblages of quartz, riebeckite, aegirine and biotite. This granite displays higher thermal values in band 11 than in band 14 (Table 2) due to the very low content of quartz and high content of K-feldspars (Ninomiya et al. 2005). In the emissivity image (Fig. 4b), this granitic variety shows dark grey colour in band 10. The three mentioned granitic types are well

discriminated from the surrounding rocks in the false colour composite emissivity image (b10, b11, b12) in RGB (Fig. 4d).

The ultramafic rocks in the study area are represented by serpentinite and talc-carbonate rocks. Serpentinite consists essentially of antigorite and chrysotile replaced by carbonate, talc and magnesite, while talc-carbonate rocks consist mainly of magnesite and antigorite (Kamal El Din 1993). The major carbonate minerals show spectral emissivity minima in ASTER band 14 attributed to the C–O bending mode. This feature in the emissivity spectra shifts to shorter wavelengths (i.e. magnesite) depending on the type of the carbonate minerals (Ninomiya et al. 2005). As shown in Table 2 and Fig. 3a,

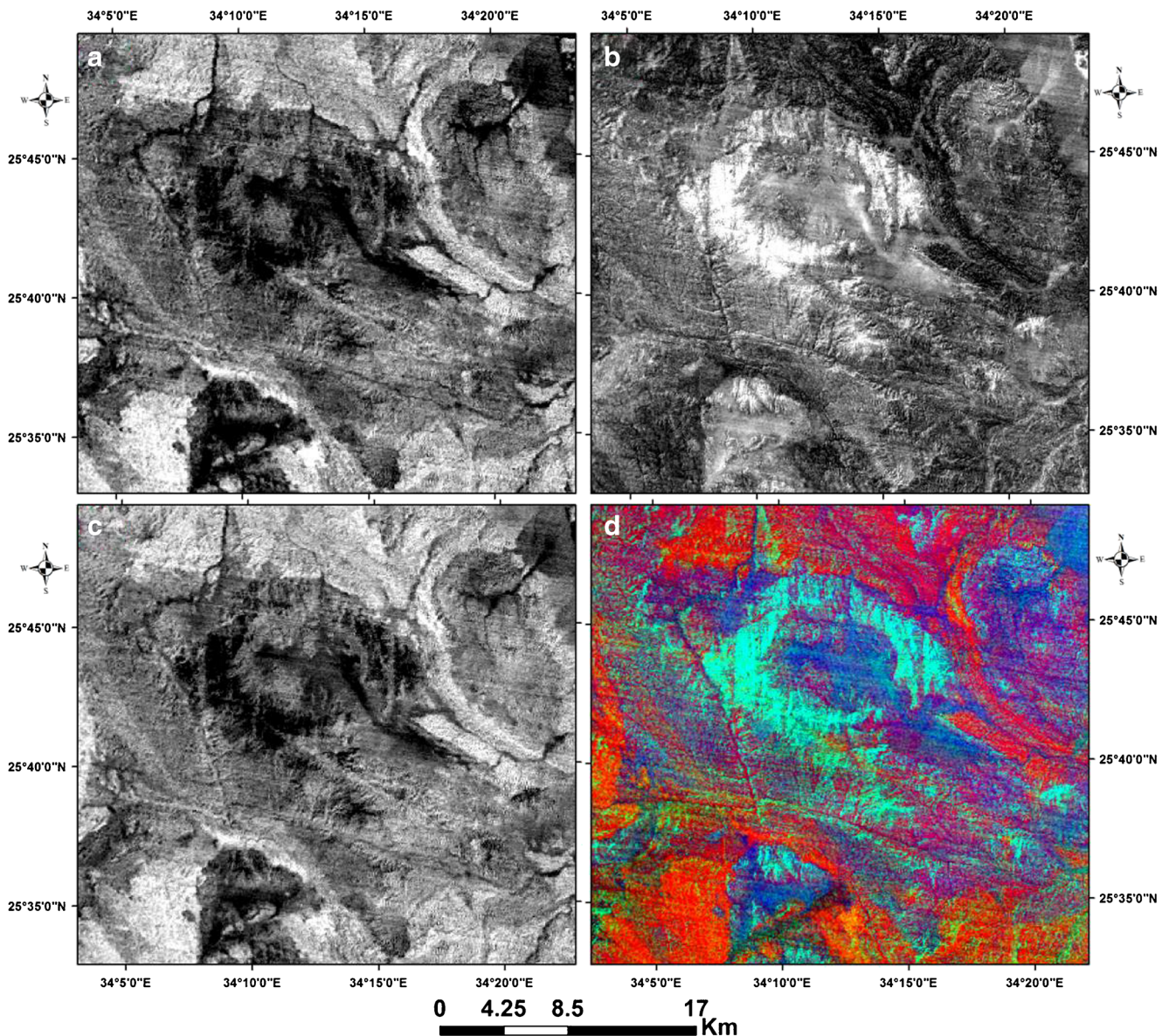


**Fig. 5** **a** Grey scale band ratio image ( $b_{12}/b_{13}$ ) of ASTER thermal data differentiates the serpentinite talc-carbonate rocks with very bright regions. **b** Band ratio ( $b_{10} \times b_{11}/b_{13} \times b_{14}$ ) of the same ASTER data discriminates the granitic intrusions rocks as very bright regions. **c** Grey scale band ratio ( $b_{12}/b_{14}$ ) of the same ASTER data emphasizes the

metavolcanic rocks with *light grey* regions. **d** False colour band ratio image ( $b_{12}/b_{13}$ ,  $b_{10} \times b_{11}/b_{13} \times b_{14}$ ,  $b_{12}/b_{14}$ ) in R, G and B for best discrimination of granitic rocks (*greenish cyan*), metavolcanics (*dark red*) and serpentinite (*bright red*)

the serpentinite and talc-carbonate rocks in the study area have higher emissivity values in ASTER bands 10 and 11 than in bands 12 to 14 due to the presence of carbonate and magnesite associated and replacing serpentine minerals.

The schistose metavolcanics along Wadi Umm Gheig and northeast of Gabal El-Sibai area range in composition from metabasalts, meta-andesites and metadacites. Petrographically, these rocks consist mainly of variable amounts of plagioclase, quartz, hornblende and chlorite (Kamal El Din 1993). They exhibit a relatively lower emissivity value in ASTER band 11 than that in bands

10 and 12 (Fig. 3b) comparable with the characteristic behaviour of the intermediate rocks (Ninomiya et al. 2005). However, they have minimum spectral values shifted to longer wavelengths at ASTER band 14 due to the presence of carbonate minerals (Ninomiya et al. 2005) incorporated as talc-carbonate slices within the metavolcanic schist. For comparison, the TIR spectral characteristics of all mapped rock units are shown in Fig. 3f.

The applied ASTER thermal band ratio image ( $b_{10} \times b_{11}/b_{13} \times b_{14}$ ) discriminates all granitic rocks with bright colour



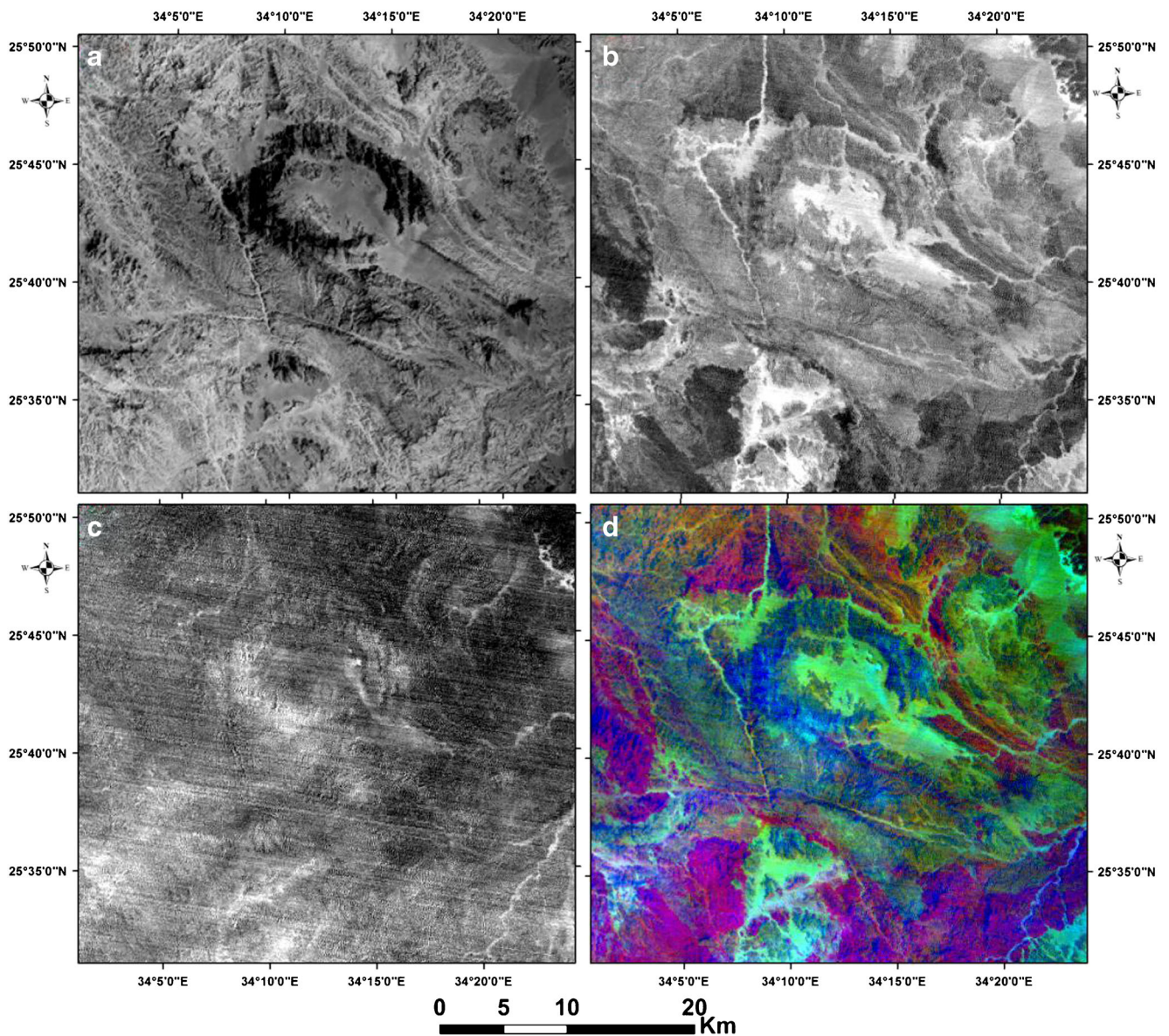


**Fig. 6** a–c Grey scale bands of principal component transformation images of ASTER thermal data (PC1, PC2 and PC3). d False colour composite image (PC1, PC2 and PC3) in RGB showing the variation of the discriminated granitic varieties (see Fig. 7) for more visual interpretation details

areas (Fig. 5b), while the surrounding serpentinites and metavolcanics show darker colour areas. On the other hand,

the alkali-feldspar granite displays slightly darker tone than the other granitic rock types.

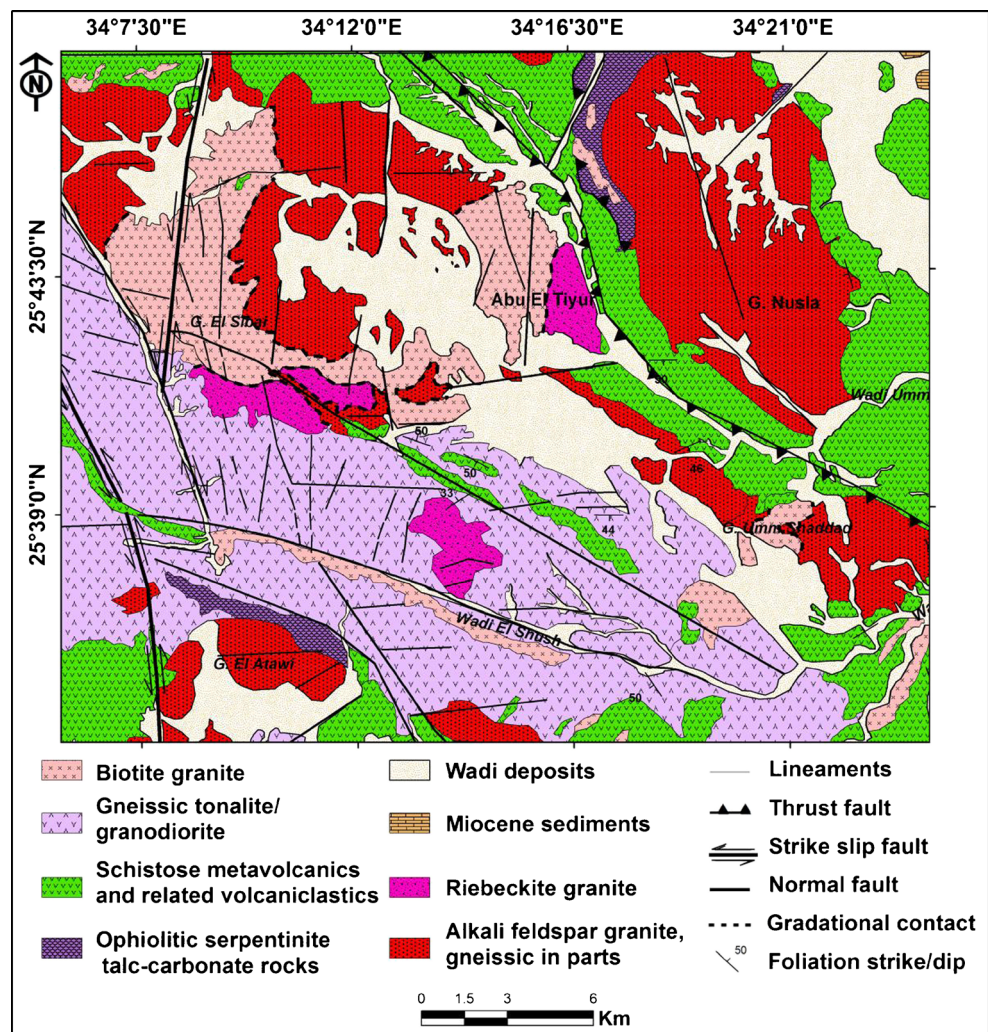
**Table 3** Eigenvector loadings and eigenvalues of PCs for the derivative ASTER emissivity bands

|              | PC1      | PC2      | PC3      | PC4      | PC5      |
|--------------|----------|----------|----------|----------|----------|
| B10          | 0.63     | -0.70    | 0.28     | 0.14     | -0.00    |
| B11          | 0.60     | 0.21     | -0.75    | -0.12    | -0.00    |
| B12          | 0.47     | 0.64     | 0.58     | -0.10    | 0.00     |
| B13          | 0.03     | 0.19     | -0.06    | 0.93     | 0.28     |
| B14          | -0.00    | -0.06    | 0.01     | -0.27    | 0.95     |
| Eigenvalues  | 72.88505 | 4.891007 | 0.016048 | 0.012686 | 0.000673 |
| Information% | 92.39072 | 7.571454 | 0.020626 | 0.016305 | 0.000865 |

The band ratio image (b12/b14) differentiates the highly schistose metavolcanics by their dark grey colour (Fig. 5c). Figure 5a shows the serpentinite-talc-carbonate rocks as having a very bright colour on the ASTER thermal band ratio image (b12/b13).

The newly proposed false colour combination ASTER thermal image of band ratios (b12/b13, b10×b11/b13×b14 and b12/b14) distinguishes the serpentinite-talc-carbonate rocks as very bright red colour. Most of the granitic rocks show greenish cyan colour, and the metavolcanics display greenish red colour (Fig. 5d). Based on the PCA eigenvector analyses (Table 3 and Fig. 6), the PC1 image (Fig. 6a) correlates with granitic rocks as positive eigenvector values (0.63)

**Fig. 7** Geological map of the El-Sibai Abu Tiyyur area modified after Fowler et al. (2007) and Kamal El Din (1993) using the ASTER thermal data



and serpentinite with positive eigenvector values (0.60) and metavolcanics with positive eigenvector values (0.47), while the PC2 image (Fig. 6b) correlates with the serpentinite, granitic and metavolcanic rock units. This is verified by negative eigenvector loadings for serpentinite (−0.70) and positive eigenvector value (0.64) for the metavolcanics and granitic intrusion with positive values (0.21). PC3 image has positive eigenvector loadings for riebeckite granite (−0.75) and positive value (0.58) for alkali-feldspar granite and positive eigenvector value (0.28) for biotite granite. Both PC4 and PC5 show noisy data. The band combination (PC1, PC2 and PC3) of the principal component image (Fig. 6d) discriminates three different granite bodies in the El-Sibai-Abu Tiyyur granitic intrusion which are biotite granite, alkali-feldspar granite and riebeckite granite that are poorly discriminated on images of band ratios ( $b_{12}/b_{13}$ ,  $b_{10} \times b_{11}/b_{13} \times b_{14}$  and  $b_{12}/b_{14}$ ). The PC1 and PC2 grey scale images (Fig. 6a, b) do not discriminate between granitic varieties, while the PC3 grey scale image (Fig. 6c) emphasizes the alkali-feldspar granite by the dark grey tone and the riebeckite granite by

white tone, while the biotite granite is emphasized with very bright grey tone. Figure 5d shows that the biotite, alkali-feldspar and riebeckite granites are discerned by dark blue, dark green and light cyan colours, respectively.

## Conclusions

The Pan-African nappe assemblage in Umm Gheig El-Sibai-Umm Shaddad area was intruded by syn- to late- and post-tectonic granitoids. This study is concerned with the lithological mapping of the basement rocks exposed in this area with emphasis on the El-Sibai-Abu Tiyyur granitic intrusion. The interpretation is based on the data of ASTER thermal band ratios ( $b_{12}/b_{13}$ ,  $b_{10} \times b_{11}/b_{13} \times b_{14}$  and  $b_{12}/b_{14}$ ) in RGB, the average TIR spectral curves characterizing the exposed rock units as well as the quantitative/ qualitative principal component transformation (PC1, PC2 and PC3) analyses. This study reveals that the mineralogical composition of these

rocks is an effective factor controlling spectral characteristics. The results derived from this newly proposed method for lithological discrimination in the study area show consistency with the field check. Compared with the previous geological maps of the study area, the produced geological map (Fig. 7) shows some differences, which can be summarized as follows: (1) The NW–SE-trending belt located between Gabal Nusla and Gabal Abu Tiyur granitic intrusions is differentiated in the present geological map into serpentinite talc-carbonate rocks and metavolcanic schists intruded by biotite granite. These rock units were previously mapped collectively as one unit, namely tectonic mélange of serpentinite talc magnesite, pillow basaltic lava with rare microgabbro and microdiorite (EGSMA 1992; Ibrahim and Cosgrove 2001). (2) Two main different granitic intrusive bodies are discerned by Fowler et al. (2007) in the study area including (a) granitic intrusions in the ophiolitic association and (b) gneissic associations of granodiorite and granite (Umm Shaddad, Nusla and El-Shush), while this study revealed that the granitic rocks forming the intrusions of Gabals Nusla, Umm Shaddad, Al Atawi and the central part of El-Sibai slightly show the same spectral characteristics in the ASTER thermal band ratio image (Fig. 5d) due to the similarities in their mineralogical composition, although they show some differences in tectonic relations and probably age of magma differentiation. Accordingly, they are mapped as alkali-feldspar granites. (3) Petrographically, Kamal El Din (1993) identified three granitic varieties forming El-Sibai-Abu Tiyur intrusion, namely biotite granite, alkali-feldspar granite and riebeckite granite without discrimination in his geological map. In this study, these three granitic varieties are discriminated in the present geological map. This pluton is previously mapped as one unit of alkali-feldspar granite (e.g. EGSMA 1992; Kamal El Din 1993; Ibrahim and Cosgrove 2001; Abdeen 2003; Fowler et al. 2007). (4) The ophiolitic serpentinite talc-carbonate rocks and the schistose metavolcanics are well discriminated, and the boundaries between these rocks are modified in the produced geological map compared with the previous mapping of the study area. This study reveals that the applied data of ASTER thermal spectral characteristic analyses, band ratios, principal component and derivative emissivity images are helpful tools in lithological discrimination of some exposed rock units. ASTER data processing shows good correlation with fieldwork for the discriminated rock units. The analyses of ASTER TIR datasets have been found to be appropriate for the detection of the mineralogical composition of different rock units in other similar tectonically and geologically arid regions in the Eastern Desert and worldwide.

**Acknowledgments** The first author would like to express her thanks to the scientists in the Institut für Angewandte Geowissenschaften, Karlsruhe University, Germany for their valuable discussions and great help during her visit to the institute, where she was kindly invited by Prof. Reinhard Greiling and funded by DFG. Grateful thanks to Prof. Fowler for reading the manuscript and his valuable comments. Thanks also for the editor and the reviewers of this manuscript for their valuable revisions.

## References

- Abdeen MM (2003) Tectonic history of the Pan-African orogeny in Umm Gheig area, Central Eastern Desert. *Egypt J Geol* 47(1):239–254
- Abdeen MM, Greiling RO (2005) A quantitative structural study of late Pan-African compressional deformation in the Central Eastern Desert (Egypt) during Gondwana assembly. *Int Gondwana Res* 8(4):457–471
- Abdeen MM, Greiling RO, Sadek MF, Hamad SS (2014) Magnetic fabrics and Pan-African structural evolution in the Najd Fault corridor in the Eastern Desert of Egypt. *J Afr Earth Sci* 99:93–108
- Abdel-Rahman AM, El-Kibbi MM (2001) Anorogenic magmatism: chemical evolution of the Mount El-Sibai A-type complex (Egypt), and implications for the origin of within-plate felsic magmas. *Geol Mag* 138:67–85
- Aboelkhair H, Ninomiya Y, Watanabe Y, Sato I (2010) Processing and interpretation of ASTER TIR data for mapping of rare-metal-enriched albite granitoids in the Central Eastern Desert of Egypt. *J Afr Earth Sci* 58:141–151
- Abou Elmagd K, Emam A, Ali-Bik MW (2013) Chemostratigraphy, petrography and remote sensing characterization of the Middle Miocene-Holocene sediments of Ras Banas peninsula, Red Sea Coast, Egypt. *Carpathian J Earth Environ Sci* 8(3):27–42
- Abrams JM, Brown D, Lepley L, Sadowski R (1983) Remote sensing for porphyry copper deposits in Southern Arizona. *Econ Geol* 78:591–604
- Akaad, M.K., Abu El Ela, A.M., 2002. Geology of the basement rocks in the eastern half of the belt between latitudes 25° 30- and 26° 30-N Central Eastern Desert, Egypt. The Geological Survey of Egypt, Paper No. 78, EGSMA, Cairo, p. 118
- Ali-Bik MW, Taman Z, El Kalioubi B, Abdel Wahab W (2012) Serpentinite-hosted talc-magnesite deposits of Wadi Barramiya area, Eastern Desert, Egypt: characteristics, petrogenesis and evolution. *J Afr Earth Sci* 64:77–89
- Amer R, Kusky T, Ghulam A (2010) Lithological mapping in the Central Eastern Desert of Egypt using ASTER data. *J Afr Earth Sci* 56:75–82
- Amer R, Kusky T, El Mezayen A (2012) Remote sensing detection of gold related alteration zones in Um Rus area, Central Eastern Desert of Egypt. *Adv Space Res* 49:121–134
- Bregar M, Fritz H, Unzog W (1996) Structural evolution of low-angle normal faults SE of the Gebel El-Sibai Crystalline Dome; Eastern Desert, Egypt: evidence from paleopiezometry and vorticity analyses. *Zbl Geol Palaont* 3/4:243–256, Teil I, H
- Bregar M, Bauernhofer A, Pelz K, Kloetzli U, Fritz H, Neumayr P (2002) A late Neoproterozoic magmatic core complex in the Eastern Desert of Egypt: emplacement of granitoids in a wrench-tectonic setting. *Precambrian Res* 118:59–82
- Cudahy TJ, Okada K, Yamato Y, Huntington JF and Hackwell JA (2000) Mapping skarn alteration mineralogy at Yerington, Nevada, using airborne hyperspectral TIR SEBASS imaging data. ERIM Proceedings of the 14th International Conference on Applied Geologic Remote Sensing: 70–79

- EGSMA (1992) Wadi Al Barramiyah quadrangle map, Egyptian Geological Survey, Cairo. El
- El Gaby S, List FK, Tehrani R (1988) Geology, evolution and metallogenesis of the Pan African belt in Egypt. In: El Gaby S, Greiling RO (eds) *The Pan-African belt of northeast Africa and adjacent areas*. Vieweg & Sohn, Braunschweig / Wiesbaden, pp 17–68
- El Gaby S, List FK, Tehrani R (1990) The basement complex of the Eastern Desert and Sinai. In: Said R (ed) *The geology of Egypt*. Balkema, Rotterdam, pp 175–184
- El Gaby S (1983) Architecture of the Egyptian basement complex. *International Basement Tectonics Assoc., Publ.*, 5: 8
- El Gaby S, El Nady O, Khudeir A (1984) Tectonic evolution of the basement complex in the Central Eastern Desert of Egypt. *Geol Rundsch* 73:1019–1036
- El Gaby S, Khudeir AA, Asran AM (1994) Geology and geochemistry of the Pan-African volcano-sedimentary belt at Wadi Umm Gheig, Eastern Desert. *Egypt Bull Fac Sci Assiut Univ* 23:185–219
- El Ramly MF (1972) A new geological map for the basement rocks in the eastern and south Western Deserts of Egypt. *Ann Geol Surv Egypt* 2:1–18
- El-Sayed MM, Hassanen MA, Obeid MA (1999) Geochemistry and petrogenesis of Late Precambrian tonalite-granodiorite-syenogranite series at Umm Shaddad district (Egypt). *Neues Jb Miner Abh* 175:29–51
- El-Sayed MM, Mohamed FH, Fumes H, Kanisawa S (2002) Geochemistry and petrogenesis of the Neoproterozoic granitoids in the Central Eastern Desert, Egypt. *Chem Erde* 62:317–346
- Fowler AR, Khamees H, Dowidar H (2007) El-Sibai gneissic complex, Central Eastern Desert, Egypt: folded nappes and syn-kinematic gneissic granitoid sheets—not a core complex. *J Afr Earth Sci* 49: 119–135
- Fritz H, and Messner M (1999) Intramontane basin formation during oblique convergence in the eastern Desert of Egypt: magmatically versus tectonically induced subsidence. *Tectonophysics*, 145–162
- Fritz H, Dallmeyer DR, Wallbrecher E, Loizenbauer J, Hoinkes G, Neumayr P, Khudeir AA (2002) Neoproterozoic tectonothermal evolution of the Central Eastern Desert, Egypt: a slow velocity tectonic process of core complex exhumation. *J Afr Earth Sci* 34: 137–155
- Gad S, Kusky TM (2006) Lithological mapping in the Eastern Desert of Egypt, the Barramiya area, using Landsat thematic mapper (TM). *J Afr Earth Sci* 44(2006):196–202
- Gad S, Kusky TM (2007) ASTER spectral ratioing for lithological mapping in the Arabian-Nubian shield, the Neoproterozoic Wadi Kid area, Sinai, Egypt. *Gondwana Res* 11(3):326–335
- Greiling RO, Abdeen MM, Dardir AA, El Akhal H, El Ramly MF, Kamal El Din GM, Osman AA, Rashwan AA, Rice AHN, Sadek MF (1994) A structural synthesis of the Proterozoic Arabian-Nubian Shield in Egypt. *Geol Rundsch* 83:484–501
- Hamimi Z (1996) Tectonic evolution of the shield rocks of Gabal El Sibai area, Central Eastern Desert, Egypt. *Egypt J Geol* 40:423–453
- Hassan SM, Ramadan TM (2014) Mapping of the late Neoproterozoic Basement rocks and detection of the gold-bearing alteration zones at Abu Marawat-Semna area, Eastern Desert, Egypt using remote sensing data. *Arab J Geosci*. doi:10.1007/s12517-014-1562-0
- Hook SJ, Dmochowski JE, Howard KA, Rowan LC, Karlstrom KE, Stock JM (2005) Mapping variations in weight percent silica measured from multispectral thermal infrared imagery. Examples from the Hiller Mountains, Nevada, USA and Tres Virgenes-La Reforma, Baja California Sur, Mexico. *Remote Sens Environ* 95:273–289
- Hussein AAA, Ali MM, El Ramly MF (1982) A proposed new classification of the granites of Egypt. *J Volcanol Geotherm Res* 14:187–198
- Ibrahim S, Cosgrove J (2001) Structural and tectonic evolution of the Umm Gheig/El-Shush region, Central Eastern Desert of Egypt. *J Afr Earth Sci* 33:199–209
- Johnson PR, Andresen A, Collins AS, Fowler AR, Fritz H, Ghebreab W, Kusky T, Stern RJ (2011) Late Cryogenian–Ediacaran history of the Arabian–Nubian Shield: a review of depositional, plutonic, structural, and tectonic events in the closing stages of the northern East African Orogen. *J Afr Earth Sci* 61:167–232
- Kamal El Din, GM (1993) Geochemistry and tectonic significance of the Pan- African El-Sibai Window, Central Eastern Desert, Egypt. *Scientific Series of the International Bureau, Forschungszentrum Julich*, 19: 154p
- Kamal El Din GM, Khudeir AA, Greiling RO (1992) Tectonic evolution of a Pan-African gneiss culmination, Gabal El-Sibai area, Central Eastern Desert. *Egypt Zbl Geol Palaontol* 11:2637–2640, Teil I, H
- Khudeir AA, Asran AH (1992) Back-arc Wizr Ophiolites at Wadi Umm Gheig district, Eastern Desert, Egypt. *Bull Fac Sci Assiut Univ* 21: 1–22
- Khudeir AA, El Gaby S, Greiling RO and Kamal El Din GW (1992) Geochemistry and tectonic significance of polymetamorphosed amphibolites in the Gebel El-Sibai window, Central Eastern Desert, Egypt. In: *Geology of the Arab World Conference*, Cairo University, Egypt: 461–476
- Khudeir AA, El-Gaby S, Kamal El Din GM, Asran AMH, Greiling RO (1995) The pre-Pan-African deformed granite cycle of the Gabal El-Sibai swell, Eastern Desert, Egypt. *J Afr Earth Sci* 21:395–406
- Le YU L, LI X, Zhang D and Dong C (2008) Characteristics of remote sensing emission spectra of composite igneous rocks. *International Workshop on Education Technology and Training and International Workshop on Geoscience and Remote Sensing*, IEEE
- Mars JC, Rowan LC (2006) Regional mapping of phyllic-and argillic-altered rocks in the Zagros magmatic arc, Iran, using Advanced Spaceborne Thermal Emission and Reflection Radiometer (ASTER) data and logical operator algorithms. *Geosphere* 2(3): 161–186
- Moghtaderi A, Moore F, Mohammadzadeh A (2007) The application of advanced space-borne thermal emission and reflection (ASTER) radiometer data in the detection of alteration in the Chadormalu paleocrater, Bafq region, Central Iran. *J Asian Earth Sci* 30:238–252
- Ninomiya Y (2002) Mapping quartz, carbonate minerals and mafic-ultramafic rocks using remotely sensed multispectral thermal infrared ASTER data. *Proc SPIE* 5234:180–190
- Ninomiya Y, Fu B (2002) Quartz index, carbonate index and SiO<sub>2</sub> content index defined for ASTER TIR data. *J Remote Sens Soc Jpn* 22:50–61
- Ninomiya Y, Fu B (2003) Extracting lithologic information from ASTER multispectral thermal infrared data in the northeastern Pamirs. *Xinjiang Geol* 21:22–30
- Ninomiya Y, Fu B, Cudahy TJ (2005) Detecting lithology with Advanced Spaceborne Thermal Emission and Reflection Radiometer (ASTER) multispectral thermal infrared “radiance-at-sensor” data. *Remote Sens Environ* 99:127–139
- Ragab AI, El-Kalioubi B, El-Alfy Z (1993) Proliferation of tectonic assemblages and crustal evolution of the area north of Abu El-Tiyur, central Eastern Desert, Egypt. *MERC Ain Shams Univ Earth Sci Ser* 7:1–16
- Rajendran S, Nasir S, Kusky TM, Ghulam A, Gabr S, El-Ghali AKM (2013) Detection of hydrothermal mineralized zones associated with listwaenites in Central Oman using ASTER data. *Ore Geol Rev* 53: 470–488
- Rowan LC, Mars JC (2003) Lithologic mapping in the Mountain Pass, California area using Advanced Spaceborne Thermal Emission and Reflection Radiometer (ASTER) data. *Remote Sens Environ* 84(3): 350–366
- Rowan LC, Hook SJ, Abrams MJ, Mars JC (2003) Mapping hydrothermally altered rocks at Cuprite, Nevada, using the Advanced Spaceborne Thermal Emission and Reflection Radiometer (ASTER). A new satellite-imaging system. *Econ Geol* 98(5): 1019–1027

- Sabet, A.H.A., 1961. Geology and mineral deposits of Gebel El-Sibai Area, Red Sea Hills, Egypt, U.A.R. Unpubl. Ph.D. thesis, Leiden State University, the Netherlands, 189p
- Sadek MF, Hassan SM (2012) Application of Egyptsat-1 and Landsat-ETM data fusion in discrimination of volcanic and granitic rocks at Gabal Gharib area, northeastern Egypt. *Austr J Basic Appl Sci* 6(13):471–480
- Shackleton RM (1979) Evaluation and mineralization of the Arabian-Nubian Shield. In: A.M.S. Al-Shanti (ed.), Pergamon Press, Oxford, 1–16
- Stern RJ (1994) Arc assembly and continental collision in the Neoproterozoic East African orogen implications for consolidation of Gondwanaland. *Ann Rev Earth Planet Sci* 22:319–351
- Tolba ME, Ramadan TM, Abdeen MM, Gabr SS (2003) Structural controlling factors of the mineralization in the Central Eastern Desert using remote sensing data and geographic information systems. 5th International Scientific Conference (F.I.S.C), Sciences, Development and Environment, Cairo: 25–27 March, 2003
- Vaughan RG, Hook SJ, Calvin WM, Taranik JV (2005) Surface mineral mapping at Steamboat Springs, Nevada, USA, with multi-wavelength thermal infrared images. *Remote Sens Environ* 99:140–158